Particles II
Access the latest eBook →

11 Advanced Optical Metrology

Particles II

EVIDENT OLYMPUS

WILEY

Impact on Biological Systems and the Environment

This eBook is dedicated to the research of Professor David Wertheim.
In collaboration with various groups, Professor Wertheim uses confocal microscopy to analyse the impact of different types of particles on human health and the environment, with a focus on human health-hazardous particles detected with solid-state nuclear track detectors (SSNTD). Download for free, today.

EVIDENT
OLYMPUS

WILEY

FeNi@N-Doped Graphene Core–Shell Nanoparticles on Carbon Matrix Coupled with MoS₂ Nanosheets as a Competent Electrocatalyst for Efficient Hydrogen Evolution Reaction

Sayyar Ali Shah, Li Xu, Rani Sayyar, Iltaf Khan, Aihua Yuan,* Xiaoping Shen, Xiaohong Li, and Habib Ullah*

Synthesis of noble-metal-free electrocatalysts for green hydrogen production is crucial to overcoming the energy demand of modern society. One of the most competitive and alternative noble-metal-free electrocatalysts for hydrogen evolution reaction (HER) is molybdenum disulfide (MoS_2)-based composites. Herein, it is shown that MoS_2 nanosheets grow on FeNi@N-doped graphene nanoparticles/N-doped carbon matrix (FeNi@NG/NCM@MoS_2), using the hydrothermal method. FeNi@NG/NCM@MoS_2 hybrid displays outstanding HER performance with a low overpotential of 79 mV at 10 mA cm^{-2}, a small Tafel slope of 40.2 mV dec^{-1}, and high durability. First-principles density functional theory simulations confirm the electron transformation from FeNi alloy to NG surface of FeNi@NG particle and subsequently further transfer to MoS_2 nanosheets, which decrease the Gibbs free energy ($\Delta G_H{}^* \approx -0.08$ eV) and local work function for enhanced HER activities. This work highlights the understanding of electron transfer in demonstrating the kinetic reaction of the HER process and offers a new avenue for constructing efficient MoS_2-based electrocatalysts.

1. Introduction

In the last few decades, human population of the world is rapidly growing that will require a huge amount of energy source for daily life activities. The development of sustainable clean energy technologies is highly essential to meet the requirement of the modern world and simultaneously keep safe our livable environment. Hydrogen is a vital clean energy source and a valuable alternative to fossil fuels for the long-term future.[1] At present, 96% of hydrogen is produced from fossil fuels such as coal gasification and steam methane reformation process.[1,2] However, this process produces some toxic greenhouse gases including carbon dioxide,[2] that seriously affect our environment. Electrochemical water splitting is a promising green approach for clean and renewable hydrogen production and can also overcome environmental challenges.[3,4] Generally, high active electrocatalysts have been used to derive the hydrogen evolution reaction (HER) at low overpotential. The most documented highly electroactive catalyst for HER is Pt-based materials (PBM).[5,6] However, the high cost and scarcity of PBM limit its large-scale hydrogen production. Therefore, it is highly desirable to develop a highly active, environmentally friendly, low-cost, and earth-abundant elements-based electrocatalyst for HER. In this connection, some competitive noble-metal-free electrocatalysts have been reported for enhanced HER performance.[7–12]

Molybdenum disulfide (MoS_2) nanosheets are one of the emerging candidates to replace noble-metal-HER catalysts due to their low cost, remarkable performance, and excellent stability.[13–15] It is believed that HER active sites in intrinsic MoS_2 nanosheets are mostly located on exposed edges.[13] Because of rich terminating sulfur groups at the edges of monolayer or few-layer of MoS_2 nanosheets, it can display better HER performance compared to that of bulk MoS_2.[16] However, the MoS_2 nanosheets tend to agglomerate due to inherent stacking by van der Waals forces, which decreases the active sites for HER activity. The synthesis of MoS_2 nanosheets with maximum numbers of exposed active sites and nonagglomeration is an

S. A. Shah, L. Xu, R. Sayyar, I. Khan, A. Yuan
School of Environmental and Chemical Engineering
Jiangsu University of Science and Technology
Zhenjiang 212003, P. R. China
E-mail: aihua.yuan@just.edu.cn
X. Shen
School of Chemistry and Chemical Engineering
Jiangsu University
Zhenjiang 212013, P. R. China
X. Li, H. Ullah
Renewable Energy Group
College of Engineering
Mathematics and Physical Sciences
University of Exeter
Penryn Campus, Penryn, Cornwall TR10 9FE, UK
E-mail: hu203@exeter.ac.uk

ADVANCED
SCIENCE NEWS
www.advancedsciencenews.com

ADVANCED
MATERIALS
INTERFACES
www.advmatinterfaces.de

ideal strategy. The hierarchical morphology of MoS_2 nanosheets is a better choice for exposing more active sites on the edges for the enhanced HER performance.[17]

Another fundamental problem of MoS_2 nanosheets is their semiconducting nature,[18] which restricts the electron transfer to reach the catalytic active sites and combines with adsorbed H^+ in an acidic medium to produce hydrogen molecule.[19,20] So, the poor catalytic activity of observed for MoS_2 nanosheets in the HER process. The introduction of conductive materials into MoS_2 can enhance the electron transfer rate to active edges of MoS_2 and can improve the HER performance.[19,20] Recently, MoS_2 nanosheets are grown on various carbon materials such as graphene, carbon nanotubes, hollow carbon sphere, carbon cloth, etc. for enhanced HER performances.[21–24] Nevertheless, it is found that the conductivity of graphitic carbons severely damages with growth or deposition of semiconductor materials and oxygen functionalization. Carbon encapsulated metals nanomaterials can provide an opportunity to maintain high electrical conductivity for MoS_2 nanosheets by penetrating electrons from core metal particles to carbon surface and further transferring them to semiconducting MoS_2 nanosheets.[25] Moreover, carbon can be used as a substrate for the growth of MoS_2 as well as protection for metallic core metals nanoparticles in both acidic,[26,27] and alkaline media,[28] in electrochemical HER performance. It is highly desired to develop a method to anchor MoS_2 nanosheets on carbon encapsulated metals nanomaterials for high HER performance.

Here, we reported that MoS_2 nanosheets grow on FeNi@N-doped graphene on/in N-doped carbon matrix (FeNi@NG/NCM@MoS$_2$) by hydrothermal method. The MoS_2 nanosheets grow both FeNi@N-doped graphene (FeNi@NG) and N-doped carbon (NDC) matrix and formed hierarchical morphology with highly exposed active sites for HER activity. The FeNi@NG/NCM@MoS$_2$ hybrid exhibits outstanding HER performance with a low overpotential of 79 mV at 10 mA cm^{-2} and a small Tafel slope of 40.2 mV dec^{-1}. Besides, our electrocatalysts are highly stable and durable in acidic media. Finally, we performed density functional theory (DFT) calculations for our experimentally observed FeNi@NG/NCM@MoS$_2$ electrocatalyst. The simulated Gibbs free energy, electron difference density, and electronic properties of the FeNi@NG/NCM@MoS$_2$ model demonstrate and validate the role of electron transfer in the excellent HER electrocatalytic activity.

2. Experimental Section

2.1. Synthesis of FeNi@NG/NCM

The FeNi@NG/NCM was prepared according to the previous report with some modifications.[29] Briefly, 0.5 g of Ni(CH$_3$COO)$_2$·4H$_2$O, 0.6 Fe(NO$_3$)$_3$·9H$_2$O, 0.2 g of polyvinylpyrrolidone, and 1 g of urea were ground together. The powder was dissolved in ethanol and kept at room temperature to evaporate the solvent. Then, the reaction mixture was heated at 750 °C in a tube furnace for 45 min under an Ar atmosphere. The sample was collected and treated with 1 M H$_2$SO$_4$ solution for 6 h to remove FeNi without N-doped graphene shells.

2.2. Synthesis of FeNi@NG/NCM@MoS$_2$

The FeNi@NG/NCM@MoS$_2$ hybrids structure was prepared by the hydrothermal method. 0.1 g of as-prepared FeNi@NG/NCM and 0.1 g of (NH$_4$)$_2$MoS$_4$ precursor were dispersed in water, followed by sonication. The reaction mixture was transferred to a 25 mL Teflon-lined stainless-steel autoclave and heated at 200 °C for 10 h. The precipitate was obtained by centrifugation and washed with distilled water and ethanol, respectively. The final product was obtained after drying in the vacuum oven for 20 h.

2.3. Synthesis of NCM@MoS$_2$

The NCM was prepared without Ni(CH$_3$COO)$_2$·4H$_2$O, and Fe(NO$_3$)$_3$·9H$_2$O salts. The NCM@MoS$_2$ was prepared with the same procedure as followed for FeNi@NG/NCM@MoS$_2$.

2.4. Synthesis of MoS$_2$ Nanosheets Sphere

The MoS$_2$ spheres were also prepared by hydrothermal method. 0.1 g of (NH$_4$)$_2$MoS$_4$ precursor was dissolved in water by sonication and subsequent similar steps were used for the synthesis of FeNi@NG/NCM@MoS$_2$ nanocomposites.

2.5. Characterizations

In order to observe the morphologies and microstructures of the as-prepared products, they were characterized by scanning electron microscope (SEM Hitachi S-4800) and transmission electron microscope (TEM, JEM-2010). The elemental mapping images of the sample were observed by energy-dispersive X-ray (EDX) spectroscopes, attached with TEM. The crystal phase compositions of products were analyzed by an X-ray diffractometer (XRD, Bruker D-8 Advanced diffractometer). Raman spectrometer (a JYHR800, 532 nm laser source) was used to acquire Raman spectra of samples. Brunauer–Emmett–Teller (BET) surface area was measured from the specific surface porosity analyzer (ASAP2020 Mack instruments). The elemental composition and valence state of products were analyzed by X-ray photoelectron spectroscopy (XPS, Thermo ESCALAB 250XI system with Al Kα X-ray as an excitation source).

2.6. Electrochemical Measurements

All the catalytic measurements for HER performance were analyzed by a three-electrode system on an electrochemical workstation (CHI 760D, Chen Hua Instruments Co. Ltd., Shanghai, China). A glassy carbon electrode was used as a working electrode, while a carbon rod (demission: dimeter = 3 mm, length = 50 mm), and saturated calomel electrode (SCE) were used as a counter, and reference electrode, respectively. Catalyst sample (4 mg) and 5 wt% of Nafion solution (40 µL) were dispersed in ethanol (960 µL) by sonicating to obtain a homogeneous ink. For electrochemical tests, 5 µL of ink was dropped onto a glassy carbon electrode and waited to dry in the air before

**ADVANCED
SCIENCE NEWS**
www.advancedsciencenews.com

**ADVANCED
MATERIALS
INTERFACES**
www.advmatinterfaces.de

being used. The cyclic voltammograms (CVs) with a scan rate of 100 mV s^{-1} were performed in 0.5 m H$_2$SO$_4$ solution for 50 cycles. The linear sweep voltammetry (LSV) curve was measured in the same solution at a scan rate of 5 mV s^{-1}. For the stability test, continuous 1500 CV cycles were measured at a scan rate of 100 mV s^{-1} from −0.6 to 0 V versus SCE, and remeasure LSV curve. The chronoamperometric carves were obtained for 10 h to judge the long-term stability of the sample. For the electrochemical active surface area of catalysts, the double-layer capacitances (C_{dl}) were calculated from CV cycles with a potential window of 0 and 0.1 V versus SCE at different scan rates. Electrochemical impedance spectroscopy (EIS) tests were performed in the frequency range of 100 kHz to 100 MHz with an AC voltage of 5 mV in 0.5 m H$_2$SO$_4$ solution.

2.7. Computational Methodology

DFT simulations were carried out for the model of experimentally observed electrocatalysts, using Quantum ATK,[30] and the results were analyzed on VESTA and vnl Version 2019.12.[30] To model the experimentally observed MoS$_2$ nanosheets grow on FeNi@N-doped graphene/N-doped carbon matrix (FeNi@NG/NCM@MoS$_2$), first, i) a single layer of 5% N-doped C matrix (NCM) was modeled, ii) then a single layer of MoS$_2$ sheet, iii) followed by 5% nitrogen-doped graphene shell which encapsulated the FeNi nanoparticles (FeNi@NG), iv) and finally these three species were attached on each other and built the FeNi@NG/NCM@MoS$_2$ hybrid electrocatalyst. All these model structures are shown in Figure S1 (Supporting Information).

The HER activity of FeNi@NG/NCM, MoS$_2$, NCM@MoS$_2$, and FeNi@NG/NCM@MoS$_2$ was calculated in the form of Gibbs free energy, using DFT calculations. Subsequently, one H atom was attached to the surfaces of these four species and the systems were allowed to be relaxed. Although the size of the theoretical models was smaller than their experimentally observed species, the essential effect on the electronic structure was already captured by this simple geometry. The generalized gradient approximation with the Perdew–Burke–Ernzerhof exchange-correlation functional and double Zeta Polarized basis set was employed for the structural and energy optimization. In this work, a linear combination of atomic orbitals method was used for Fe, Ni, Mo, S, C, N, and H atoms.[31] A 7 × 7 × 3 Monkhorst–Pack k-point sampling was adopted for structural optimization and 7 × 7 × 7 for the electronic property simulations.

As reported in the previous work, the overall HER mechanism over the surface of the electrocatalyst was evaluated with a three-state diagram, consisting of an initial H$^+$ state, an intermediate H* state, and 1/2H$_2$ as the final product. As is known, the H* free energy of (ΔG_{H*}) is a key for describing the HER activity of the electrocatalyst. An electrocatalyst with a positive value ΔG_{H*} shows low kinetics of adsorption of hydrogen. While a negative ΔG_{H*} value is responsible for low kinetics of release of a hydrogen molecule. So, the acceptable value of ΔG_{H*} must be zero; i.e., the ΔG_{H*} value of PM-based catalyst such as Pt is near-zero as $\Delta G_{H*} \approx 0.09$ eV.[32] The ΔG_{H*} can be determined with the help of Equation (1)

$$\Delta G_{H*} = \Delta E_{H*} + \Delta E_{ZPE} - T\Delta S_H \tag{1}$$

In Equation (1), ΔE denotes the total energy change which can be calculated from the DFT simulations, ΔZPE and ΔS are the changes in zero-point energy and entropy, respectively. And T is the room temperature (298.15 K). As reported elsewhere, the theoretical working potential is independent of the pH, which is due to the free energies of the elementary reactions varying in the same way as pH. So, the potential determining step remains constant. To simplify the theoretical simulated data we set the pH = 0. The free energy of hydrogen at standard conditions is assumed as the energy of 1/2H$_2$. The entropy of the H$_2$ is taken from the NIST database[33]

$$\Delta E_{H*} = E_{(H*)} - E_{(*)} - 1/2E_{H2} \tag{2}$$

Here, $E_{(H*)}$ and $E_{(*)}$ are calculated from the DFT which is of the given surface with and without H adsorption, respectively, and E(H$_2$) is the DFT energy of a molecular H$_2$ in the gas phase. After all, the ΔE_{H*} is the binding energy of adsorbed hydrogen. Therefore, Equation (1) can be rewritten as

$$\Delta G_{H*} = \Delta E_{H*} + 0.37 \text{ eV} \tag{3}$$

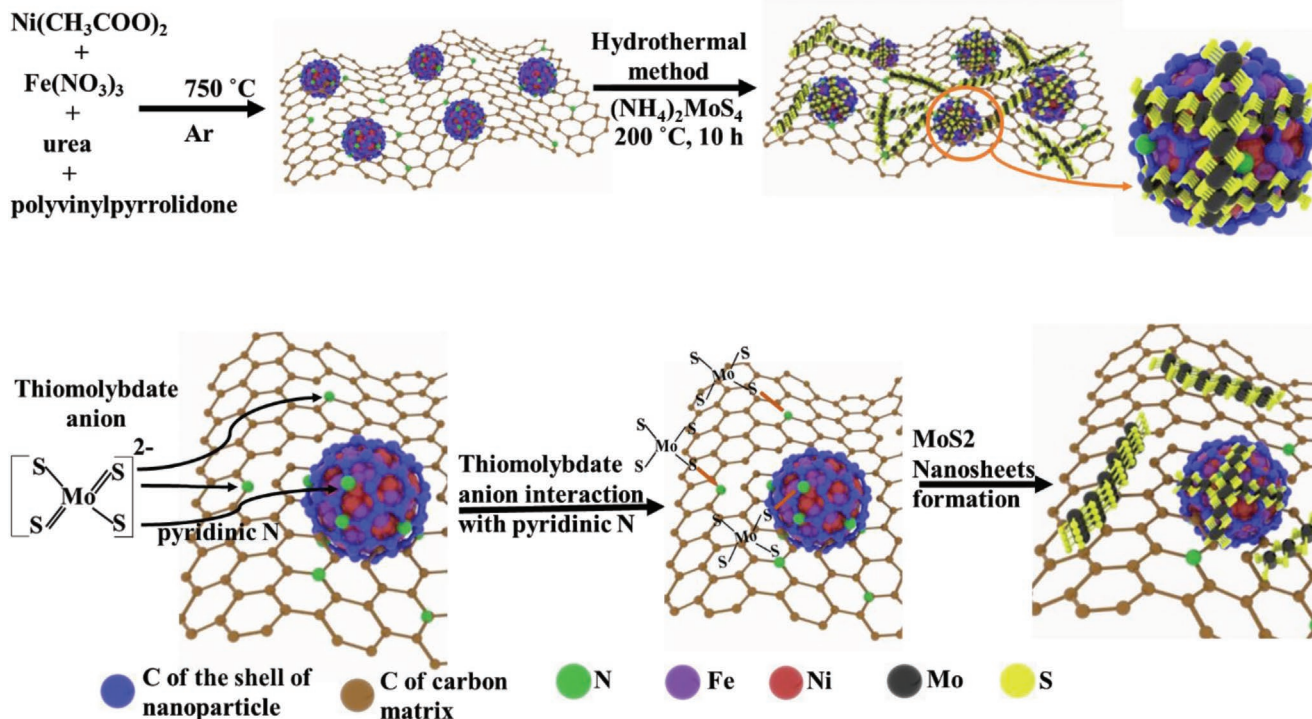Equation (3) is the final equation for calculating the free energy of H.

3. Results and Discussion

3.1. Synthesis and Characterization

Scheme 1 shows the synthesis process of FeNi@NG/NCM@MoS$_2$ hybrid electrocatalyst The FeNi@NG/NCM was prepared according to the previous report.[29] The FeNi@NG/NCM were dispersed in water and then (NH$_4$)$_2$MoS$_4$ precursor was added to the dispersion. The (NH$_4$)$_2$MoS$_4$ dissociated in the thiomolybdate anions (MoS$_4$)$^{2-}$ and ammonium cation (NH$_4$)$^+$ in hydrothermal conditions. The thiomolybdate anions are adsorbed pyridinic N-doping sites of the FeNi@NG/NCM by electrostatic attraction,[22] and subsequently act as nucleation sites for the growth into MoS$_2$. On further reaction, the MoS$_2$ starts to grow on FeNi@NG/NCM. Most MoS$_2$ nanosheets vertically grow on FeNi@NG/NCM. This vertical growth might be possibly due to its lamellar structure.

A flaky type structure can be clearly observed in SEM images of FeNi@NG/NCM sample as shown in **Figure 1**a. The areas of these flaky structures are several square micrometers. On further magnification, the surface of the flaky structure is relatively rough, and some nanoparticles can be seen as shown in Figure 1b. When (NH$_4$)$_2$MoS$_4$ precursor is treated without FeNi@NG/NCM sample in hydrothermal conditions, the sphere-like structures are obtained (Figure S2a, Supporting Information). Actively, the sphere-like structure is consisted of nanosheets and suggests the agglomeration of MoS$_2$ (Figure S2b, Supporting Information).

TEM images of FeNi@NG/NCM sample are shown in Figure 1c, where it can be seen that the flaky structure is of several micrometers. Well-defined nanoparticles can be seen on/in the flaky structure (Figure 1c,d). The size of these nanoparticles varies from 60 to 6 nm. The EDX spectrum reveals that FeNi@NG/NCM sample is composed of Ni, Fe, N, C, and

ADVANCED
SCIENCE NEWS
www.advancedsciencenews.com

ADVANCED
MATERIALS
INTERFACES
www.advmatinterfaces.de

Scheme 1. Schematic illustration of the synthesis process of FeNi@NG/NCM@MoS$_2$ composite catalyst.

O elements (Figure S3, Supporting Information). It indicts that FeNi@NG/NCM samples consist of FeNi alloy and N-doped carbon. The high-resolution TEM (HRTEM) of nanoparticles further reveals the core-shell structure (Figure 1e,f). The core is consisted of crystalline particles with a lattice spacing of about 0.205 nm and matches very well to that of (111) planes of cubic FeNi alloy, while the shell consists of a layer structure with a spacing of about 0.34 nm, which corresponds to graphite carbon. The carbon matrix is composed of both graphitic and amorphous carbon.
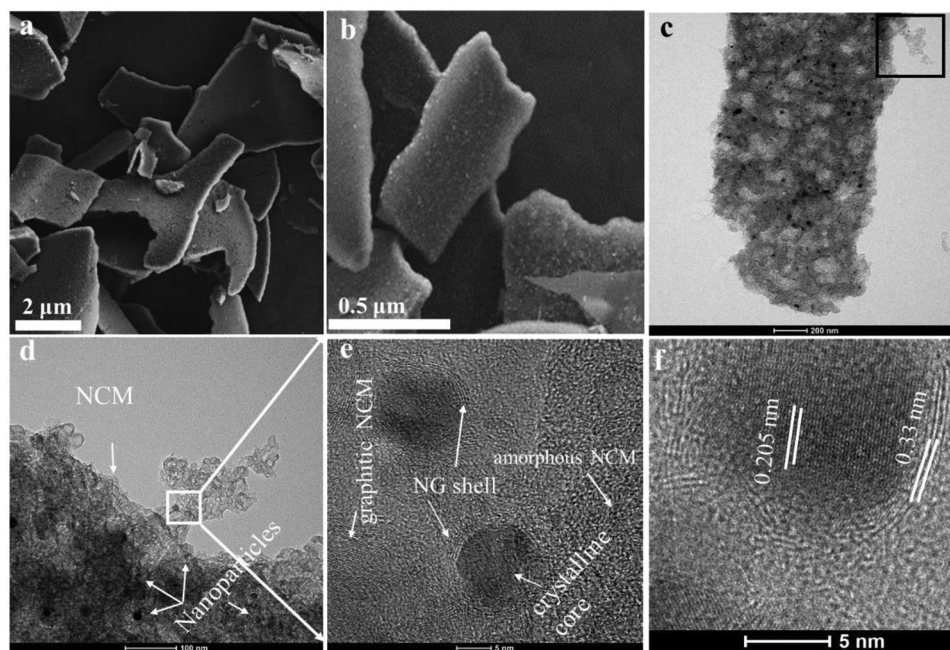

Figure 1. a,b) SEM images of FeNi@NG/NCM sample, c,d) TEM images of the FeNi@NG/NCM product, and e,f) HRTEM images of FeNi@NG/NCM sample.
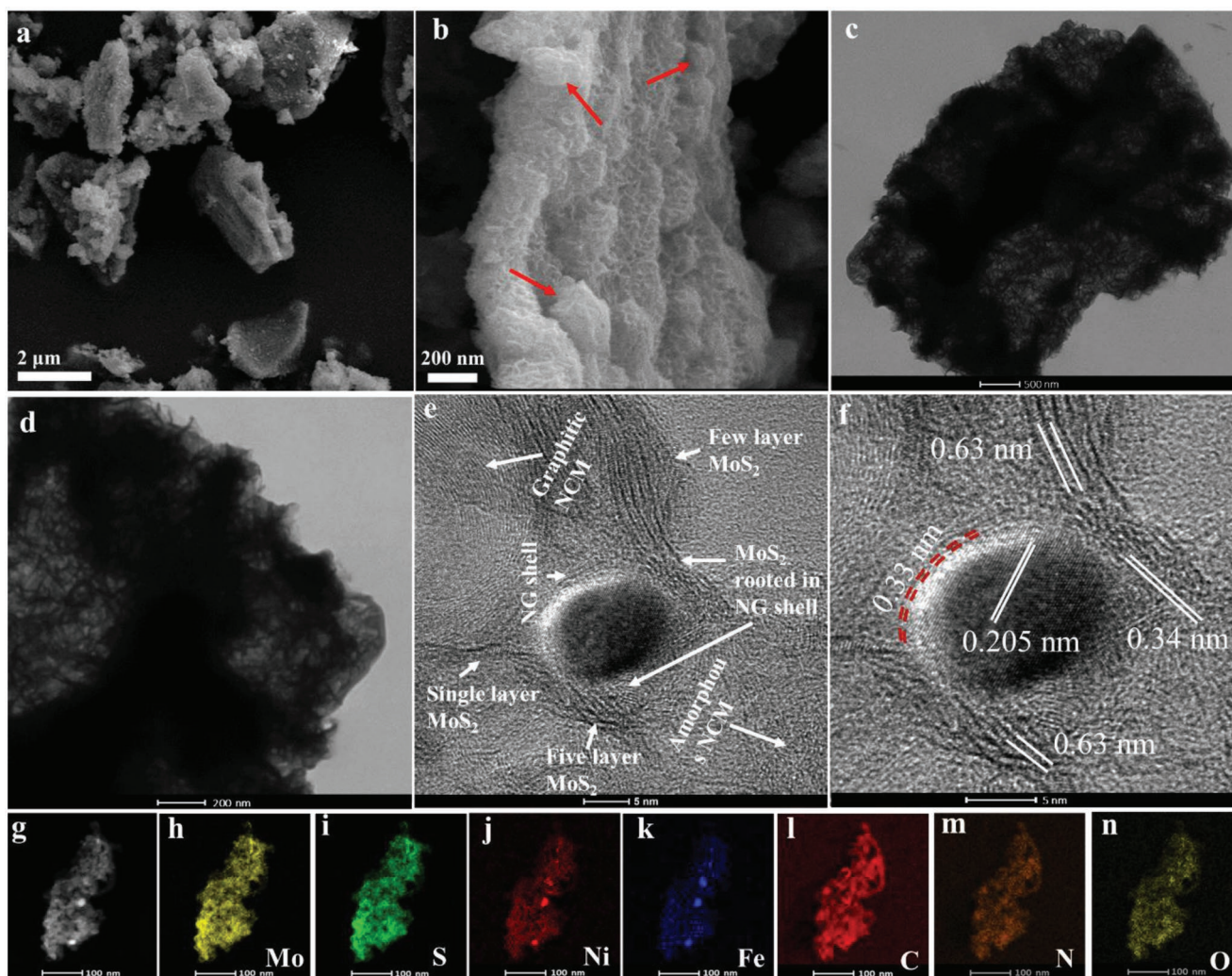
**ADVANCED
SCIENCE NEWS**

www.advancedsciencenews.com

**ADVANCED
MATERIALS
INTERFACES**

www.advmatinterfaces.de

Figure 2. a,b) SEM, c,d) TEM, and e,f) HRTEM images of FeNi@NG/NCM@MoS$_2$ hybrid. g) Dark-field TEM image of FeNi@NG/NCM@MoS$_2$ hybrid. Elemental mapping images of h) Mo, i) S, j) Ni, k) Fe, l) C, m) N, and n) O of FeNi@NG/NCM@MoS$_2$ sample.

After the treatment of FeNi@NG/NCM sample with (NH$_4$)$_2$MoS$_4$) precursor, the SEM images show that the surface morphology of the flaky type structure of FeNi@NG/NCM is changed to hierarchical as shown in **Figure 2**a. Actually, the hierarchical structure denotes that MoS$_2$ nanosheets grow on FeNi@NG/NCM. The hierarchical sphere-like (shown by red arrows) morphology indicates MoS$_2$ nanosheets, which are grown on FeNi@NG nanoparticles, while the MoS$_2$ nanosheets are also observed on NCM (Figure 2b). This suggests that hierarchical vertically MoS$_2$ nanosheets are grown on N-doped carbon of both FeNi@NG and NCM. From careful observation, it can be observed that these nanosheets are very small, and basal to edges is very high. The edges of most MoS$_2$ nanosheets are highly exposed. Recently, it is reported that hierarchical morphology MoS$_2$ and its highly exposed edges are beneficial for enhanced HER performance.[17,34] The MoS$_2$ nanosheets are scattered on the surface of the NCM in the NCM@MoS$_2$ composite, which is different from the FeNi@NG/NCM@MoS$_2$ hybrid (Figure S4a,b, Supporting Information).

Analysis of TEM images also confirms that the surface morphology of FeNi@NG/NCM is changed. The MoS$_2$ nanosheets grow on FeNi@NG/NCM can be clearly observed in Figure 2c. The FeNi@NG/NCM sample is more transparent without nanoparticles places, while it becomes darker in the nanoparticles (Figure 2d). MoS$_2$ nanosheets can be observed on NCM in the NCM@MoS$_2$ sample as shown in Figure S4c,d of the Supporting Information. HRTEM images of the FeNi@NG/NCM@MoS$_2$ hybrid are shown in Figure 1e,f, where the single or few-layer structures observed on the graphitic carbon shell of FeNi@NG nanoparticle can be observed. The interlayer spacing is about 0.63 nm, which is consistence with bulk MoS$_2$. The graphitic and amorphous carbon phases can also be seen in the NCM sample. So, it is inferred that nanoparticles have a well-defined lattice plane encapsulated in the carbon shell. The lattice planes spacing 0.204 nm are related to cubic FeNi alloy. The interlayer spacing of shells is about 0.34 nm, which matches to graphitic carbon. These images clearly display that MoS$_2$ nanosheets are grown on the FeNi@NG/NCM. The few layers MoS$_2$ nanosheets can be seen on NCM of FeNi@NG/NCM@MoS$_2$
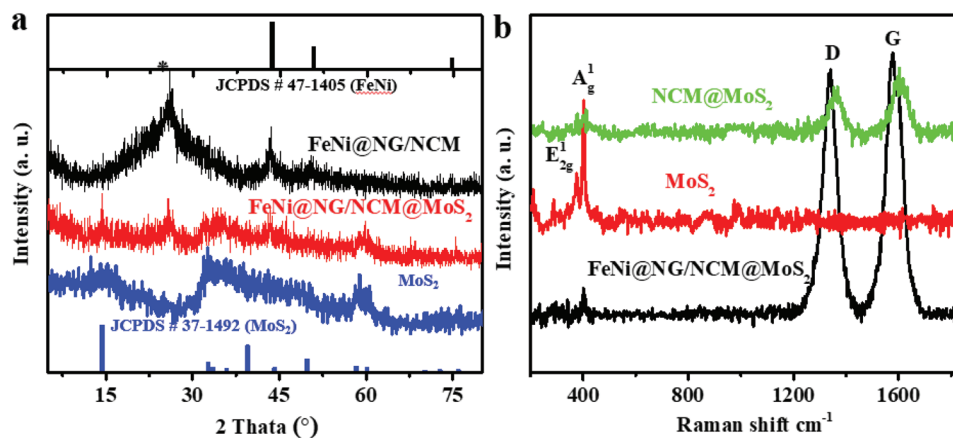
ADVANCED
SCIENCE NEWS
www.advancedsciencenews.com

ADVANCED
MATERIALS
INTERFACES
www.advmatinterfaces.de

Figure 3. a) XRD patterns of the as-synthesized FeNi@NG/NCM sample, FeNi@NG/NCM@MoS$_2$ hybrid, and pure MoS$_2$ nanosheets. The peak denoted by star (*) represents the diffraction of carbon materials. b) Raman spectra of FeNi@NG/NCM@MoS$_2$, NCM@MoS$_2$ hybrid, and MoS$_2$ nanosheets.

sample (Figure S5, Supporting Information). The dark field TEM images (Figure 2g) and corresponding elemental mapping images of Mo, S, Ni, Fe, C, N, and O of FeNi@NG/NCM sample are shown in Figure 2h–n. The signals of Mo and S elements are slightly more obvious on the particle's surfaces compared to that of NCM. The elemental mapping of Ni and Fe images shows the presence of FeNi alloy. The signals of C and N elements indicate N-doped in carbon materials. The homogenous signals of O arise from the surface oxidation of sample.

The crystal structures of FeNi@NG/NCM and FeNi@NG/NCM@MoS$_2$ were analyzed by powder X-ray diffraction (XRD) technique as shown in **Figure 3**a. The FeNi@NG/NCM sample shows four discernable diffraction peaks. The three diffraction peaks at 43.62°, 50.67°, and 74.89° can be well-matched with (111), (200), and (220) of cubic FeNi alloy (JCPDS No. 47–1405), while the broad peak center at 26.05 associated to the (002) diffraction of carbon materials. The broadening of the peak suggests the presence of some amorphous carbon in FeNi@NG/NCM sample. After MoS$_2$ nanosheets were rooted in FeNi@NG/NCM sample, some new peaks emerged. These new peaks are at about 14.5°, 32.9°, and 58.2°, which can be assigned to (002), (100), and (110) crystallographic planes of hexagonal 2H-MoS$_2$ (JCPDS No. 37–1492). The peaks for hexagonal 2H-MoS$_2$ are more obvious in the pure MoS$_2$ nanosheets. The results and analysis of XRD data also validate and confirm the successful synthesis of the hybrid of FeNi@NG/NCM and MoS$_2$ nanosheets. The prominent peaks for MoS$_2$ nanosheets were not observed in NCM@MoS$_2$ sample, which may be due to the high peak intensity of the NCM (Figure S6, Supporting Information).

In addition, the Raman spectral analysis of FeNi@NG/NCM@MoS$_2$, NCM@MoS$_2$ hybrids, and MoS$_2$ nanosheets, shown in Figure 3b, was also performed. FeNi@NG/NCM@MoS$_2$ hybrids show intense D- and G-bands peaks at 1346 and 1584 cm^{-1}, respectively, while the D- and G-bands peaks were observed for NCM@MoS$_2$ sample at 1356 and 1595 cm^{-1}, respectively. These peaks confirm the characteristic bands of carbonaceous materials.[35] The intensity ratio (I_D/I_G) of FeNi@NG/NCM@MoS$_2$ and NCM@MoS$_2$ are about 0.9 and 1.03, respectively, and show relativity graphitization of carbon. The weak peaks are observed at 373 and 401 cm^{-1}, which

can be assigned as in-plane (E$^1_{2g}$) and out-of-plane (A^1_g) vibration modes of MoS$_2$, respectively,[36,37] while these peaks are more intense in the pure MoS$_2$ nanosheets. The frequency difference (Δk) can be used to estimate the number of MoS$_2$ layers in nanosheets. Δk of MoS$_2$ in all samples is about 27 cm^{-1} and suggests that the number of MoS$_2$ layers is more than 5.[36,37] The BET results show the specific surface area of MoS$_2$ (Figure S7a, Supporting Information), FeNi@NG/NCM@MoS$_2$ (Figure S7b, Supporting Information), and NCM@MoS$_2$ (Figure S7c, Supporting Information) are 11, 18, and 33.2 cm^3 g^{-1}, respectively.

The XPS spectrum was acquired for the surface elemental composition and chemical state of the samples. The survey XPS spectra of FeNi@NG/NCM@MoS$_2$ and pure MoS$_2$ nanosheets are shown in Figure S8a of the Supporting Information. The FeNi@NG/NCM@MoS$_2$ composites show peaks for Fe, Ni, Mo, S, C, N, and O elements, while MoS$_2$ nanosheets contain Mo, S, C, and O elements. The high-resolution XPS spectrum of the Fe 2p region has main peaks at about 707.2 and 720.3 eV, which can be associated with Fe 2p$_{3/2}$ and Fe 2p$_{1/2}$ bands of zero valance of metallic Fe (**Figure 4**a).[38,39] The peaks at about 710.3 and 723.7 eV are related to Fe 2p$_{3/2}$ and Fe 2p$_{1/2}$ signals of oxidized iron and/or satellite of iron.[29,40] The Ni 2p XPS spectrum shows two intense peaks at 853.2 and 871.2 eV, which correspond to Ni^0 2p$_{3/2}$ and Ni^0 2p$_{1/2}$ of metallic Ni, respectively (Figure 4b).[41,42] The Mo 3d spectrum of FeNi@NG/NCM@MoS$_2$ hybrid shows four peaks (Figure 4c). The peak at 225.25 eV matches the binding energy of the S 2s band.[43,44] The well-defined peaks at 228 and 231.31 eV correspond to Mo 3d$_{5/2}$ and Mo 3d$_{3/2}$ bands of the Mo^{4+} oxidation state of the MoS$_2$ compound.[45,46] The weak and broad peaks centered at 234.3 eV are due to oxidation of Mo to Mo^{6+}.[46] The Mo 3d$_{5/2}$ and Mo 3d$_{3/2}$ bands of pure MoS$_2$ nanosheets peaks at about 228.18 and 231.40 eV show Mo^{4+} oxidation state, respectively. The XPS spectrum of the S 2p region of FeNi@NG/NCM@MoS$_2$ hybrid shows pair of peaks at 162.11 and 160.8 eV of S 2p$_{1/2}$ and S 2p$_{3/2}$ spin–orbit doublets of S^{2-} species, respectively (Figure 4d),[43,44,47] while S 2p$_{1/2}$ (162.28 eV) and S 2p$_{3/2}$ (161. eV) peaks of pure MoS$_2$ nanosheets are observed which have slightly high binding energies. The shifting toward lower binding energy of Mo and S
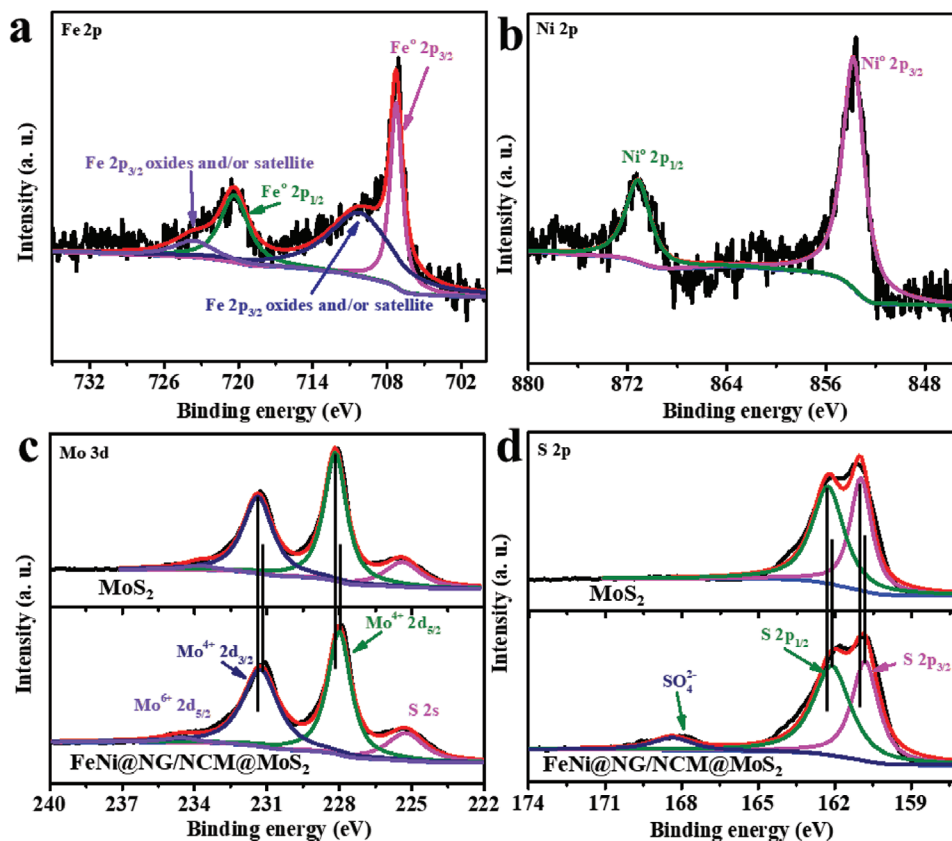
**ADVANCED
SCIENCE NEWS**

www.advancedsciencenews.com

**ADVANCED
MATERIALS
INTERFACES**

www.advmatinterfaces.de

Figure 4. High-resolution XPS spectra of a) Fe 2p and b) Ni 2p regions of FeNi@NG/NCM@MoS$_2$ composites. c) High-resolution XPS spectra of Mo 3d, d) S 2p regions of FeNi@NG/NCM@MoS$_2$ composites and MoS$_2$ nanosheets.

atoms in FeNi@NG/NCM@MoS$_2$ hybrid compared to that of pure MoS$_2$ nanosheets suggest the interaction between MoS$_2$ nanosheets and FeNi@NG/NCM. These results also indicate a relatively high electron density on the Mo and S atoms of MoS$_2$ nanosheets in FeNi@NG/NCM@MoS$_2$ hybrid as compared to pure MoS$_2$ nanosheets. A peak at higher binding energies (168.7 eV) can be related to SO$_3^{2-}$ and/or SO$_4^{2-}$ species, possibly due to the surface oxidation of MoS$_2$.[43] The high-resolution XPS spectra of C 1s region of FeNi@NG/NCM@MoS$_2$ hybrid shows peak for C—C/C=C (284.2 eV) and N—C/C—O (≈285.5 eV) and C=O (≈287.95 eV) (Figure S8b, Supporting Information).[48,49] The high-intensity peak of C—C/C=C bonds indicates the presence of graphitic carbon in the composite after the growth of MoS$_2$ nanosheets. The N 1s spectrum show peak centered at 399.7 eV (Figure S8c, Supporting Information),[29] and it is very difficult to correctly deconvolute it into different nitrogen species. The reason behind this is the overlapping with the Mo 3p region. However, well-defined peaks for pyridinic, pyrrolic, and graphitic nitrogen have been previously observed in the XPS spectrum of FeNi@NG/NCM.[29]

3.2. Electrochemical HER

The HER performance of as-prepared samples and 20% Pt/C were measured with the help of a three-electrode system on an electrochemical workstation in 0.5 m H$_2$SO$_4$ solution. The LSV

curves of the catalysts were measured at a scan rate of 5 mV s^{-1} with iR correction (**Figure 5**a). As usual, 20% Pt/C catalyst shows the best HER performances and required an overpotential of 35 mV at a current density of 10 mA cm^{-2}. The MoS$_2$, NCM@MoS$_2$, and FeNi@NG/NDM samples display poor HER performance with an overpotential of 191, 212, and 365 mV at a current density of 10 mA cm^{-2}, respectively (Table S1, Supporting Information). Upon growth of MoS$_2$ nanosheets in FeNi@NG/NCM sample, the overpotential significantly decreased to 79 mV at a current density of 10 mA cm^{-2}. This HER performance of FeNi@NG/NCM@MoS$_2$ catalyst is 2.42, 2.79, and 6.42 times that of MoS$_2$, NCM@MoS$_2$, and FeNi@NG/NCM samples, respectively. Furthermore, a physical mixture (PM) of FeNi@NG/NDM sample and MoS$_2$ nanosheets with a 1:1 ratio was investigated for HER performance. PM also shows poor HER performance at 325 mV at a current density of 10 mA cm^{-2}. The FeNi@NG/NCM@MoS$_2$ catalyst shows better performance than those of other as-prepared catalysts and also the better or comparable performance with reported MoS$_2$-based catalysts (Table S2, Supporting Information). This suggests that the enhanced HER performance is due to the synergistic effect between FeNi@NG/NCM and MoS$_2$ nanosheets.

In order to estimate the HER activities of the investigated samples, the Tafel plot analyses were studied (Figure 5b). The Tafel slopes of catalysts are obtained from LSV carves by fitting them in the Tafel equation. Generally, the smaller value of the Tafel slope of catalysts is believed to be useful for practical application. The
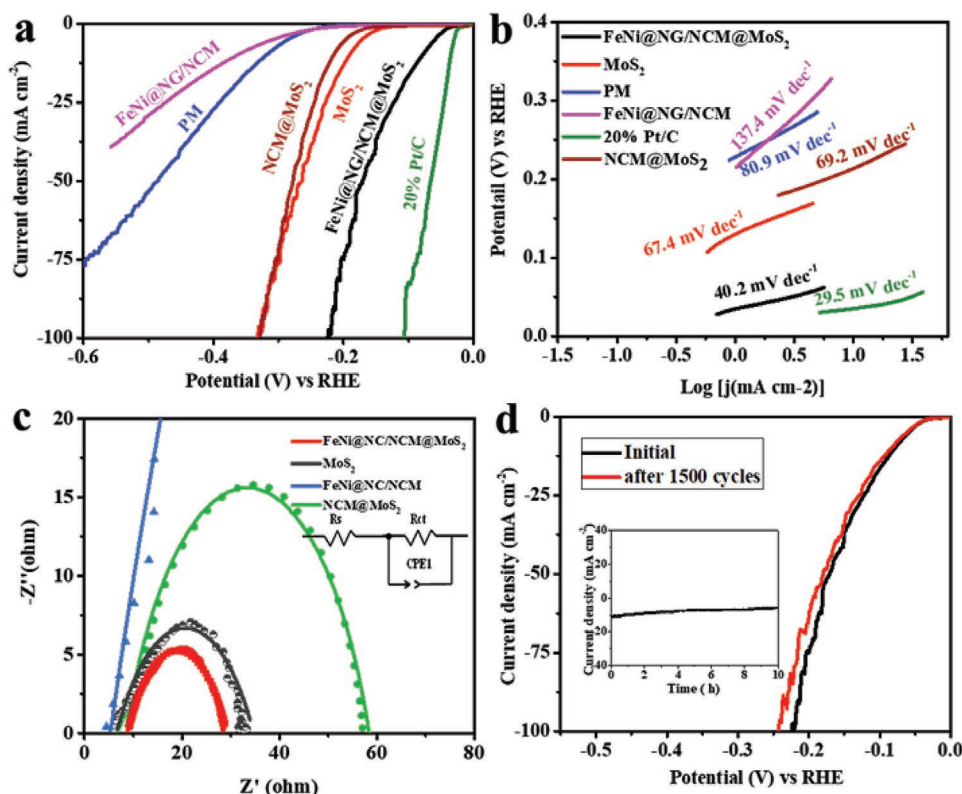
ADVANCED
SCIENCE NEWS
www.advancedsciencenews.com

ADVANCED
MATERIALS
INTERFACES
www.advmatinterfaces.de

Figure 5. a) LSV curves and b) their corresponding Tafel plots of commercial 20% Pt/C, PM, and as-prepared catalysts. c) The Nyquist plots and inset represent the equivalent circuit, which is used for R_{ct} determination. d) LSV curves of FeNi@NG/NCM@MoS$_2$ catalyst before and after 1500 CV cycles predict the stability and the inset shows the amperometric (i–t) curve FeNi@NG/NCM@MoS$_2$ hybrid.

20% Pt/C catalyst displays a small Tafel slope of 29.5 mV dec^{-1}. Among other tested samples, the FeNi@NG/NCM@MoS$_2$ catalyst demonstrates the smallest Tafel slope (40.2 mV dec^{-1}) and most effective kinetics for hydrogen production. The Tafel slope of MoS$_2$ (67.4 mV dec^{-1}), NCM@MoS$_2$ (69.2 mV dec^{-1}), PM (90.8 mV dec^{-1}), and FeNi@NG/NDM (137.4 mV dec^{-1}) catalysts are higher and comparatively slower reaction kinetics for HER. To study the rate-determining step of HER in acidic media, the HER mechanism comprises of three basic reactions, Volmer reaction (H$_3$O$^+$ + e$^-$ → H$_{ads}$ + H$_2$O, initial discharge step, and Tafel slope ≈120 mV dec^{-1}), Heyrovsky reaction (H$_3$O$^+$ + H$_{ads}$ + e$^-$ → H$_2$ + H$_2$O, electrochemical desorption step and Tafel slope ≈40 mV dec^{-1}), and the Tafel reaction (H$_{ads}$ + H$_{ads}$ → H$_2$, recombination step and Tafel slope ≈ 30 mV dec^{-1}).[43,50–52] From Tafel slope values, the rate-limiting step for HER is either Volmer–Heyrovsky or Volmer–Tafel reaction in acidic conditions. The Tafel slope value of FeNi@NG/NCM@MoS$_2$ hybrid is (40.2 mV dec^{-1}), and may follow the Volmer–Heyrovsky rection. Possibly the rate-determining step is an electrochemical desorption step.

The exchange current density (J_o) was obtained from the extrapolation of the Tafel equation.[43,53] Exchange current density of FeNi@NG/NCM@MoS$_2$, MoS$_2$, NCM@MoS$_2$, PM, FeNi@NG/NCM, and 20% Pt/C are 1.1 × 10^{-1}, 1.4 × 10^{-2}, 2.8 × 10^{-2}, 1.2 × 10^{-3}, 2.5 × 10^{-2}, and 3.8 × 10^{-1} mA cm^{-2}, respectively (Figure S9, Supporting Information). Among the tested catalysts, 20% Pt/C has the highest exchange current

density of 3.8 × 10^{-1} mA cm^{-2}. The exchange current density of FeNi@NG/NCM@MoS$_2$ is slightly lower than that of 20% Pt/C and higher compared to the remaining samples.

The electrochemical double-layer capacitances (C_{dl}) of the investigated samples were calculated from CVs and their electrochemical surface area is estimated as shown in Figure S10 of the Supporting Information. The C_{dl} value of samples are in the order of FeNi@NG/NCM@MoS$_2$ (7.2 mF cm^{-2}) > MoS$_2$ (4.9 mF cm^{-2}) > NCM@MoS$_2$ (4.3 mF cm^{-2}) > FeNi@NG/NCM (1.2 mF cm^{-2}). Comparative analysis of the C_{dl} values of these samples led to indicate that the active sites are larger for FeNi@NG/NCM@MoS$_2$ hybrid than those of FeNi@NG/NCM and MoS$_2$ nanosheets. So, the results suggest that the HER catalytic activity is mostly due to MoS$_2$ nanosheets instead of FeNi@NG/NCM product. Besides, MoS$_2$ nanosheets in FeNi@NG/NCM@MoS$_2$ hybrid are highly exposed to HER catalytic activity and easily accessible to electrolytes compared to that of pristine MoS$_2$ nanosheets.

Furthermore, the EIS of these catalysts was measured as shown in Figure 5c. The Nyquist plots were fitted with an equivalent circuit (inset of Figure 5c). The charge transfer resistance (R_{ct}) values are 20.32, 28.71, 52.37, and 417.7 Ω for FeNi@NG/NCM@MoS$_2$, MoS$_2$, NCM@MoS$_2$, and FeNi@NG/NCM samples, respectively. R_{ct} value of the M@NDC@MoS$_2$ hybrids is smaller than those of MoS$_2$ and FeNi@NG/NCM catalyst. This suggests that efficient charge transfer occurs at the electrode/electrolyte interface and hence improves catalytic performance.

Another important aspect of an electrocatalyst is stability. So, the catalyst with long-term stability can be used for practical hydrogen production. The stability of FeNi@NG/NCM@MoS$_2$ sample was tested by performing 1500 continuous CV cycling in 0.5 M H$_2$SO$_4$ solution and comparable with reported composites catalysts (Table S2, Supporting Information). The LSV curves of the catalyst before and after 1500 cycles are shown in Figure 5d. It can be analyzed that only small decay in HER performance especially at lower current density is observed compared to the initial one. This indicts the high stability of the prepared catalyst. Moreover, the same sample was characterized by TEM, HRTEM, and XPS after 1500 HER performance. The flaky structure with hierarchical morphology of FeNi@NG/NCM@MoS$_2$ sample can still be observed in TEM images after 1500 HER performance (Figure S11a,b, Supporting Information). The HRTEM image shows that the FeNi@NC nanoparticles and MoS$_2$ nanosheets are observed in the composite (Figure S11c, Supporting Information). These results confirm the long-term stability of the prepared catalyst. However, the structure of MoS$_2$ nanosheets is slightly damaged during the stability test compared to the fresh sample. The XPS survey spectrum also confirms the existence of Mo, S, Fe, Ni, C, N, and O elements in the composite (Figure S12a, Supporting Information). The peak intensity of Mo^{6+} and SO$_4^{2-}$ species in XPS spectra of the post-HER sample increased which indicates the further oxidation of these elements (Figure S12b,c, Supporting Information). Furthermore, the XPS spectra confirm the presence of metallic Ni and Fe with zero valence states after 1500 cycles (Figure S12d,e, Supporting Information), however, the surfaces of these elements are oxidized as can be observed from the oxidation peaks. The XPS spectrum of C is not obviously changed in the post-HER sample and suggests the high stability of carbon materials (Figure S12f, Supporting Information). Moreover, chronoamperometric analysis was performed to test the long-term stability of FeNi@NG/NCM@MoS$_2$ sample. It is found that the current density loss was about 12.8% after 10 h, which validates the long-term stability of the catalyst.

3.3. First-Principles Electronic Properties

As discussed earlier, first-principles DFT studies were performed to countercheck the enhanced HER activity of FeNi@NG/NCM@MoS$_2$. The NG encapsulated FeNi nanoparticles on N-doped carbon matrix interacted with MoS$_2$ nanosheet (for details see Computational Methodology section, Supporting Information). The free energy for H adsorption (ΔG_{H*}) was simulated over the surface of the observed FeNi@NG/NCM@MoS$_2$, FeNi@NG/NCM, MoS$_2$, and NCM@MoS$_2$ (see Figure S1, Supporting Information). The DFT simulated ΔG_{H*} values of these four species are shown in **Figure 6**a and Table S3 (Supporting Information), where the ΔG_{H*} value of FeNi@NG/NCM, NCM@MoS$_2$, MoS$_2$, and FeNi@NG/NCM@MoS$_2$ are −0.87, −0.14, −0.11, and −0.08 eV, respectively. Generally, an efficient electrocatalyst must have reasonable ΔG_{H*} to overcome the reaction barriers of the HER process, in the adsorption and desorption stages. Comprehensive analyses of Figure 6 led to conclude that the ΔG_{H*} value of FeNi@NG/NCM@MoS$_2$ is ideal, and very close to the thermodynamic limit value (vide supra). These

simulated Gibbs free energies further confirm and validate the efficient performance of the FeNi@NG/NCM@MoS$_2$ electrocatalyst for HER. The high activity of FeNi@NG/NCM@MoS$_2$ can be regarded due to the ideal electrostatic interaction of hydrogen with the surface of MoS$_2$ of FeNi@NG/NCM (Figure S13f, Supporting Information). Besides, the ΔG_{H*} value of FeNi@NG/NCM is very high (−0.87 eV). The reason behind this is the strong adsorption energy (−1.24 eV) of H* that subsequently obstructs the HER process and reduces the performance of the catalyst. From Table S3 of the Supporting Information, it can be analyzed that the hydrogen adsorption energy for FeNi@NG/NCM, MoS$_2$, NCM@MoS$_2$, and FeNi@NC/NCM@MoS$_2$ are −1.24, −0.51, −0.48, and −0.45 eV, respectively. So, the stronger ΔG_{H*} of hydrogen adsorption for FeNi@NG/NCM, MoS$_2$, NCM@MoS$_2$ hinders the hydrogen desorption process which finally reduces the overall HER process. The excellent HER activity of FeNi@NC/NCM@MoS$_2$ hybrid is due to the interaction of H and S at the surfaces of MoS$_2$ of the FeNi@NC/NCM@MoS$_2$, where H$^+$ is attached. The main reason behind the excellent catalytic activity of FeNi@NC/NCM@MoS$_2$ is the electron transfer mechanism. The transfer of electrons occurs from FeNi alloy core to NG shell of FeNi@NG nanoparticle and then to MoS$_2$ nanosheet in FeNi@NG/NCM@MoS$_2$. This electron transfer phenomenon can be seen in Figure 6b and Figure S14 (Supporting Information), where the electron density on MoS$_2$ surface becomes moderately increased and attracts protons, leading to the efficient evolution of hydrogen molecules. Possibly, some electrons may be electron transferred from the FeNi@NG particles to NCM and then to MoS$_2$ nanosheets. So, FeNi alloy has a key role in this electron transformation and enhances the activity of MoS$_2$ in FeNi@NG/NCM@MoS$_2$. On the other hand, the intercharge transferring phenomenon in FeNi@NG/NCM is at its peak which offers strong attractive forces for proton. So, the excited H* cannot be easily desorbed from the surface of the catalyst which reduces the HER performance. In the case of NCM@MoS$_2$, the hydrogen adsorption energy is −0.48 eV, which is still higher than that of FeNi@NC/NCM@MoS$_2$, responsible for lower HER performance as listed in Table S3 of the Supporting Information.

In addition, the efficient HER activity of FeNi@NC/NCM@MoS$_2$ may be due to an excellent interaction of FeNi@NC/NCM@MoS$_2$ nanoparticles with MoS$_2$ nanosheets. The partial density of the state plot of FeNi@NC/NCM@MoS$_2$ is shown in Figure 6c, where the bonding orbitals of Ni and Fe have strong hybridization in the region of −10 to 0 eV. While the antibonding orbitals of Fe, Ni, Mo, S, N, and C have mutual orbital overlapping in the energy range of 0 to 10 eV. The improved orbital hybridizations of these bonding and antibonding orbitals are responsible for the excellent charge transferring and overall stability of MoS$_2$ in FeNi@NC/NCM@MoS$_2$. Moreover, the existence of FeNi alloy within the NG shell and its interaction with MoS$_2$ results in extra features near the Fermi level. So, this charge is transferred from FeNi alloy core to NG shell, and then between FeNi@NC/NCM and MoS$_2$ sheet. All these charges transferring consequently reduce the Fermi level of FeNi@NC/NCM@MoS$_2$. The work function can be determined from the reciprocal of Fermi energy. The work function decreases from 4.40 (FeNi@NG/NCM) to 3.56 eV (FeNi@NC/NCM@MoS$_2$) as can be analyzed in Table S3 of the Supporting
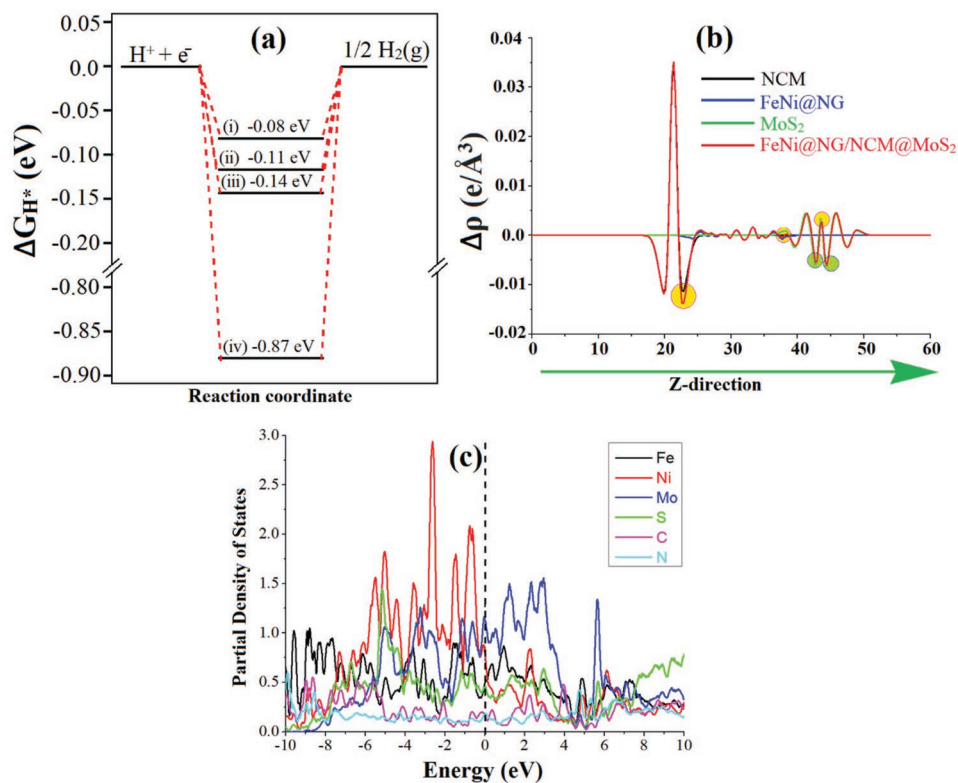
Figure 6. a) Gibbs free energy (ΔG_{H*}) of HER process of FeNi@NG/NCM@MoS$_2$ (i), NCM@MoS$_2$ (ii), MoS$_2$ (iii), and FeNi@NG/NCM (iv). b) Average electron density difference ($\Delta\rho$) along the Z-direction for NCM (black line), FeNi@NG (blue line), MoS$_2$ (green line), and FeNi@NC/NCM@MoS$_2$ (red line). The green and yellow circle-shaded areas indicate electron donation and accumulation, respectively, and c) partial density of states plots of FeNi@NC/NCM@MoS$_2$ and the Fermi energy is set to 0 eV.

Information. In order to clarify this statement, the electron density difference distribution is simulated which is shown in the inset of Figure S13 of the Supporting Information.

In summary, charge transfer creates a local dipole at the interface that subsequently decreases the local work function and improves the electrocatalytic activity and stability of the FeNi@NC/NCM@MoS$_2$. So, the optimum ΔG_{H*} of hydrogen adsorption over FeNi@NC/NCM@MoS$_2$ is due to high DOS near the Fermi level and minimum work function of the FeNi@NC/NCM@MoS$_2$.

4. Conclusion

In summary, comprehensive experimental and theoretical studies are performed for the synthesis and fabrication of a stable, cheap, and environmentally friendly electrocatalyst for HER. First, we prepared FeNi@NG/NCM@MoS$_2$ hydride with the help of the hydrothermal method. MoS$_2$ nanosheets were successfully grown on both FeNi@NC and NCM. It is found that FeNi@NG/NCM@MoS$_2$ catalyst shows enhanced electrocatalytic activity for HER performance with a low overpotential of 79 mV at 10 mA cm^{-2}, a small Tafel slope of 40.2 mV dec^{-1}, and high durability. From the DFT simulations, it is found that the enhanced HER electrocatalytic activity of FeNi@NG/NCM@MoS$_2$ is due to electron transformation from FeNi@NG to MoS$_2$ nanosheets. This work emphasizes

the understanding of electron transfer in demonstrating the kinetic reaction of the HER process and offers a new avenue for constructing efficient MoS$_2$-based electrocatalysts. Finally, DFT simulations were carried out to confirm and validate the excellent catalytic activities of FeNi@NG/NCM@MoS$_2$.

Supporting Information

Supporting Information is available from the Wiley Online Library or from the author.

Conflict of Interest

The authors declare no conflict of interest.

[1] S. Kampouri, K. C. Stylianou, *ACS Catal.* **2019**, *9*, 4247.

[2] Q. Wang, K. Domen, *Chem. Rev.* **2020**, *120*, 919

[3] Y. M. Shi, B. Zhang, *Chem. Soc. Rev.* **2016**, *45*, 1781

[4] Q. Ding, B. Song, P. Xu, S. Jin, *Chem* **2016**, *1*, 699.

[5] Q. Cheng, C. Hu, G. Wang, Z. Zou, H. Yang, L. Dai, *J. Am. Chem. Soc.* **2020**, *142*, 5594.

[6] H. Xu, H. Shang, C. Wang, Y. Du, *Adv. Funct. Mater.* **2020**, *30*, 2000793.

[7] G. Yasin, S. Ibraheem, S. Ali, M. Arif, S. Ibrahim, R. Iqbal, A. Kumar, M. Tabish, M. A. Mushtaq, A. Saad, H. Xu, W. Zhao, *Mater. Today Chem.* **2022**, *23*, 100634.

[8] Y. L. S. Cui, X. Tan, K. F. Xiao, S. L. Zhao, N. M. Bedford, Y. F. Liu, Z. C. Wang, K. H. Wu, J. Pan, W. H. Saputera, S. Cheong, R. D. Tilley, S. C. Smith, J. Yun, L. Dai, D.-W. Wang, *ACS Energy Lett.* **2020**, *5*, 3560.

[9] L. Yu, L. B. Wu, S. W. Song, B. McElhenny, F. H. Zhang, S. Chen, Z. F. Ren, *ACS Energy Lett.* **2020**, *5*, 2681,

[10] Z. Fang, L. Peng, Y. Qian, X. Zhang, Y. Xie, J. J. Cha, G. Yu, *J. Am. Chem. Soc.* **2018**, *140*, 5241.

[11] S. A. Shah, G. Zhu, X. Shen, L. Kong, Z. Ji, K. Xu, H. Zhou, J. Zhu, P. Song, C. Song, A. Yuan, X. Miao, *Adv. Mater. Interfaces* **2018**, *11*, 1801093.

[12] S. A. Shah, X. Shen, M. Xie, G. Zhu, Z. Ji, H. Zhou, K. Xu, X. Yue, A. Yuan, J. Zhu, Y. Chen, *Small* **2019**, *15*, 1804545.

[13] T. F. Jaramillo, K. P. Jorgensen, J. Bonde, J. H. Nielsen, S. Horch, I. Chorkendorff, *Science* **2007**, *317*, 100.

[14] C. Y. Jian, W. T. Hong, Q. Cai, J. Li, W. Liu, *Appl. Catal., B* **2020**, *266*, 118649.

[15] H. Khan, S. A. Shah, W. u. Rehman, F. Chen, *Adv. Mater. Interfaces* **2021**, *9*, 2101294.

[16] D. Voiry, J. Yang, M. Chhowalla, *Adv. Mater.* **2016**, *28*, 6197.

[17] J. Zhang, S. H. Liu, H. W. Liang, R. H. Dong, X. L. Feng, *Adv. Mater.* **2015**, *27*, 7426.

[18] R. Kappera, D. Voiry, S. E. Yalcin, B. Branch, G. Gupta, A. D. Mohite, M. Chhowalla, *Nat. Mater.* **2014**, *13*, 1128.

[19] Z. H. Deng, L. Li, W. Ding, K. Xiong, Z. D. Wei, *Chem. Commun.* **2015**, *51*, 1893.

[20] X. Y. Xu, X. F. Dong, Z. J. Bao, R. Wang, J. G. Hu, H. B. Zeng, *J. Mater. Chem. A* **2017**, *5*, 22654.

[21] P. Gnanasekar, D. Periyanagounder, J. Kulandaivel, *Nanoscale* **2019**, *11*, 2439.

[22] D. J. Li, U. N. Maiti, J. Lim, D. S. Choi, W. J. Lee, Y. Oh, G. Y. Lee, S. O. Kim, *Nano Lett.* **2014**, *14*, 1228.

[23] M. C. He, J. Y. Lei, C. W. Zhou, H. Y. Shi, X. D. Sun, B. Gao, *Mater. Res. Express* **2019**, *6*, 7.

[24] Z. C. Xiang, Z. Zhang, X. J. Xu, Q. Zhang, C. W. Yuan, *Carbon* **2016**, *98*, 84

[25] S. A. Shah, L. Xu, R. Sayyar, T. Bian, Z. Liu, A. Yuan, X. Shen, I. Khan, A. Ali Tahir, H. Ullah, *Chem. Eng. J.* **2022**, *428*, 132126.

[26] J. Deng, P. J. Ren, D. H. Deng, X. H. Bao, *Angew. Chem., Int. Ed.* **2015**, *54*, 2100.

[27] M. Tavakkoli, T. Kallio, O. Reynaud, A. G. Nasibulin, C. Johans, J. Sainio, H. Jiang, E. I. Kauppinen, K. Laasonen, *Angew. Chem., Int. Ed.* **2015**, *54*, 4535

[28] Y. Xu, W. G. Tu, B. W. Zhang, S. M. Yin, Y. Z. Huang, M. Kraft, R. Xu, *Adv. Mater.* **2017**, *29*, 1605957.

[29] S. A. Shah, Z. Ji, X. Shen, X. Yue, G. Zhu, K. Xu, A. Yuan, N. Ullah, J. Zhu, P. Song, X. Li, *ACS App. Energy Mater.* **2019**, *2*, 4075.

[30] S. Smidstrup, T. Markussen, P. Vancraeyveld, J. Wellendorff, J. Schneider, T. Gunst, B. Verstichel, D. Stradi, P. A. Khomyakov, U. G. Vej-Hansen, *J. Phys.: Condens. Matter* **2019**, *32*, 015901.

[31] G. Kresse, D. Joubert, *Phys. Rev. B* **1999**, *59*, 1758.

[32] J. K. Nørskov, T. Bligaard, A. Logadottir, J. Kitchin, J. G. Chen, S. Pandelov, U. Stimming, *J. Electrochem. Soc.* **2005**, *152*, J23.

[33] M. W. Chase, *J. Phys. Chem. Ref. Data* **1996**, *25*, 551.

[34] X. Zheng, J. Xu, K. Yan, H. Wang, Z. Wang, S. Yang, *Chem. Mater.* **2014**, *26*, 2344.

[35] A. C. Ferrari, D. M. Basko, *Nat. Nanotechnol.* **2013**, *8*, 235.

[36] Y. F. Yu, C. Li, Y. Liu, L. Q. Su, Y. Zhang, L. Y. Cao, *Sci. Rep.* **2013**, *3*, 6.

[37] Z. Deng, H. Jiang, Y. Hu, Y. Liu, L. Zhang, H. Liu, C. Li, *Adv. Mater.* **2017**, *29*, 1603020.

[38] Y. Yang, Z. Lin, S. Gao, J. Su, Z. Lun, G. Xia, J. Chen, R. Zhang, Q. Chen, *ACS Catal.* **2016**, *7*, 469.

[39] B. K. Barman, K. K. Nanda, *ACS Sustainable Chem. Eng.* **2018**, *6*, 12736.

[40] S. W. Park, I. Kim, S. I. Oh, J. C. Kim, D. W. Kim, *J. Catal.* **2018**, *366*, 266.

[41] P. T. Liu, D. Q. Gao, W. Xiao, L. Ma, K. Sun, P. X. Xi, D. S. Xue, J. Wang, *Adv. Funct. Mater.* **2018**, *28*, 1706928.

[42] N. Ullah, W. Zhao, X. Lu, C. J. Oluigbo, S. A. Shah, M. Zhang, J. Xie, Y. Xu, *Electrochim. Acta* **2019**, *298*, 163.

[43] Y. J. Tang, Y. Wang, X. L. Wang, S. L. Li, W. Huang, L.-Z. Dong, C.-H. Liu, Y.-F. Li, Y.-Q. Lan, *Adv. Energy Mater.* **2016**, *6*, 1600116.

[44] Y. H. Chang, C. T. Lin, T. Y. Chen, C. L. Hsu, Y. H. Lee, W. Zhang, K. H. Wei, L. J. Li, *Adv. Mater.* **2013**, *25*, 756.

[45] Y. Tian, M. Zhou, Y. Pan, X. Du, Q. Wang, *Chem. Eng. J.* **2021**, *403*, 126361.

[46] Y. Chen, F. Su, H. Xie, R. Wang, C. Ding, J. Huang, Y. Xu, L. Ye, *Chem. Eng.* **2021**, *404*, 126498.

[47] V. O. Koroteev, L. G. Bulusheva, I. P. Asanov, E. V. Shlyakhova, D. V. Vyalikh, A. V. Okotrub, *J. Phys. Chem. C* **2011**, *115*, 21199.

[48] C. Song, S. Wu, X. Shen, X. Miao, Z. Ji, A. Yuan, K. Xu, M. Liu, X. Xie, L. Kong, G. Zhu, S. A. Shaha, *J. Colloid Interface Sci.* **2018**, *524*, 93.

[49] X. Han, G. He, Y. He, J. Zhang, X. Zheng, L. Li, C. Zhong, W. Hu, Y. Deng, T. Y. Ma, *Adv. Energy Mater.* **2017**, *8*, 1702222.

[50] J. F. Xie, H. Zhang, S. Li, R. X. Wang, X. Sun, M. Zhou, J. F. Zhou, X. W. Lou, Y. Xie, *Adv. Mater.* **2013**, *25*, 5807.

[51] J. Xie, J. Zhang, S. Li, F. Grote, X. Zhang, H. Zhang, R. Wang, Y. Lei, B. Pan, Y. Xie, *J. Am. Chem. Soc.* **2013**, *135*, 17881.

[52] Y. Li, H. Wang, L. Xie, Y. Liang, G. Hong, H. Dai, *J. Am. Chem. Soc.* **2011**, *133*, 7296.

[53] Y. J. Tang, M. R. Gao, C. H. Liu, S. L. Li, H. L. Jiang, Y. Q. Lan, M. Han, S. H. Yu, *Angew Chem., Int. Ed.* **2015**, *54*, 12928.